Propagative selection of tilted array patterns in directional solidification

Younggil Song, Silvère Akamatsu, Sabine Bottin-Rousseau, and Alain Karma

Phys. Rev. Materials **2**, 053403 — Published 29 May 2018

DOI: 10.1103/PhysRevMaterials.2.053403

Propagative selection of tilted array patterns in directional solidification

Younggil Song,[1] Silvère Akamatsu,[2] Sabine Bottin-Rousseau,[2] and Alain Karma[1,*]

[1] *Department of Physics and Center for Interdisciplinary Research on Complex Systems, Northeastern University, Boston, MA 02115 USA*

[2] *Sorbonne Université, CNRS-UMR 7588, Institut des NanoSciences de Paris, case courrier 840, 4 place Jussieu, 75252 Paris Cedex 05, France*

(Dated: April 30, 2018)

We investigate the dynamics of tilted cellular/dendritic array patterns that form during directional solidification of a binary alloy when a preferred-growth crystal axis is misoriented with respect to the temperature gradient. *In situ* experimental observations and phase-field simulations in thin samples reveal the existence of a propagative source-sink mechanism of array spacing selection that operates on larger space and time scales than the competitive growth at play during the initial solidification transient. For tilted arrays, tertiary branching at the diverging edge of the sample acts as a source of new cells with a spacing that can be significantly larger than the initial average spacing. A spatial domain of large spacing then invades the sample propagatively. It thus yields a uniform spacing everywhere, selected independently of the initial conditions, except in a small region near the converging edge of the sample, which acts as a sink of cells. We propose a discrete geometrical model that describes the large-scale evolution of the spatial spacing profile based on the local dependence of the cell drift velocity on the spacing. We also derive a nonlinear advection equation that predicts the invasion velocity of the large-spacing domain, and sheds light on the fundamental nature of this process. The models also account for more complex spacing modulations produced by an irregular dynamics at the source, in good quantitative agreement with both phase-field simulations and experiments. This basic knowledge provides a theoretical basis to improve the processing of single crystals or textured polycrystals for advanced materials.

PACS numbers: 68.08.-p, 05.70.Ln, 64.70.D, 81.30.Fb

I. INTRODUCTION

The directional solidification of nonfaceted dilute alloys leads to the freezing of columnar-like microstructures in the bulk solid, which are known to largely determine the properties in use of as-cast materials in metallurgy[1–3]. These microstructures are formed during growth as a trace left behind by self-organized solidification front patterns. Their main morphological features are primarily determined by the redistribution of chemical species by diffusion in the liquid and capillary effects at the propagating solid-liquid interface, which can be considered in local thermodynamic equilibrium at slow growth rate[4–14].

During directional solidification (DS), melt crystallization is performed while a sample is pulled with a velocity V in a uniaxial temperature gradient G[6–13]. When the sample is pulled from rest, the solute concentration builds up in front of the recoling planar interface that becomes morphologically unstable[4,15,16], thereby forming shallow cells that become progressively deeper. During this initial transient, cells grow competitively due to solutal interactions between neighbors and become eliminated. Surviving cells then reach a steady-state, forming a periodic array of finger-like shapes −"cells" and "dendrites"− with a primary spacing λ (typically, a few tens of micrometers), which can vary within a large interval[8–24]. In particular, phase-field (PF) simulation studies have shown that steady-state arrays of deep cells (smooth fingers) or dendrites (branched fingers) can be stable for a large range of primary spacings $\lambda_{min} < \lambda < \lambda_{max}$[19–21]. Moreover, the largest stable spacing λ_{max} is typically several fold the smallest stable spacing λ_{min} in the velocity range where arrays of deep cells or dendrites form, and V is much larger than the onset velocity V_c of morphological instability[19–21].

Pattern selection has been studied extensively both theoretically and experimentally in a thin-sample geometry[7–14]. To date, however, those studies have primarily focused on understanding what spacing is dynamically selected by the transient growth competition between neighboring cells for a well-oriented single crystal[15,16,20–22,25]. Competitive growth continuously increases the average spacing until a stable spacing is reached. Therefore, it typically selects a spacing slightly larger than λ_{min} due to the fact that the cell elimination stops when a stable spacing is reached. In practice, the spatial λ distribution along the array is rarely uniform and can be strongly influenced by the orientation of the growing crystal with respect to the temperature gradient axis both during, and well after, the initial cell elimination process. However, the long-time evolution of the array pattern towards steady-state in a large crystal as a function of its orientation remains largely unexplored.

The crystal-orientation dependency of DS front patterns originates from the sensitivity of growth shapes to the surface-tension anisotropy of the solid-liquid interface, which is well-known to select both the orientation

* a.karma@northeastern.edu

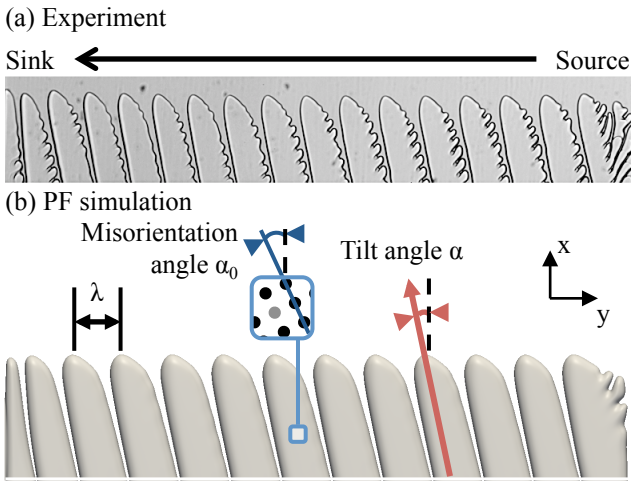

FIG. 1. Tilted-cell arrays in thin-sample directional solidification of a misoriented crystal (misorientation angle α_0) in a dilute succinonitrile-d,camphor alloy of concentration c_∞. (a) Experimental observation ($c_\infty = 0.3$ mol%; $V = 4\ \mu\mathrm{m\,s^{-1}}$; $G = 75\ \mathrm{K\,cm^{-1}}$; $\alpha_0 \approx 15.5°$) of a horizontal dimension $L_y = 2780\ \mu$m. (b) Phase-field numerical simulation ($c_\infty = 0.24$ wt%; $V = 4\ \mu\mathrm{m\,s^{-1}}$; $G = 12\ \mathrm{K\,cm^{-1}}$; $\alpha_0 = 15°$) of $L_y = 2490\ \mu$m. In these images, as well as in the following ones, the field of view covers the entire lateral width of the sample; the temperature gradient axis $\mathbf{x}$ is vertical, and the liquid is located on the top. The arrow in (a) describes drifting motion of the pattern along the lateral axis $\mathbf{y}$. α and λ are for a cell-tilt angle and a primary spacing, respectively.

and tip operating state of freely growing dendrites[26,27]. In a DS setting, however, the growth orientation is also influenced by the temperature gradient. As a result, cells/dendrites grow at an angle α with respect to the temperature gradient axis ($\mathbf{x}$ axis), which differs from the crystal misorientation angle α_0 (between the $\mathbf{x}$ axis and one of the principal crystal axes). This difference is illustrated in Fig. 1, which shows experimental and PF simulation images of tilted array patterns from the present investigation. The relationship between α and α_0 has been extensively studied previously both experimentally[28,29] and numerically[30–33]. Those studies have shown that α/α_0 is typically a monotonously increasing function of the dimensionless Péclet number $\mathrm{Pe} = \lambda/l_d$ that is largely insensitive to G, where D is the solute diffusion coefficient in the liquid and $l_d = D/V$ is the solutal diffusion length. The ratio α/α_0 varies from a value much smaller than unity for $\mathrm{Pe} \ll 1$, where the growth direction of cells is primarily determined by diffusive interactions with neighboring cells, to unity in a dendritic regime ($\mathrm{Pe} \gg 1$) where the growth direction is primarily determined by crystalline anisotropy.

This current knowledge of tilted finger patterns remains limited to a steady-state growth regime where λ is spatially uniform along the array. In this paper, we present an experimental and numerical study of the large-scale dynamics of those patterns in the generic case where λ is spatially non-uniform. Non-uniformity is expected to be generic and its origin in the setting of the growth of a single misoriented crystal is illustrated in Fig. 1. Due to the lateral drift, there is a qualitatively different operating dynamics on the two edges of the sample, each of them acting as a virtually immobile grain boundary (GB). Tilted cells travel away from the right edge in Fig. 1, referred to as the divergent GB, which acts as a source of new cells with a spacing significantly larger than λ_{min}, towards the left edge referred to as a convergent GB, which acts as a sink of cells that are eliminated when their spacing falls below λ_{min}. To investigate the pattern dynamics inside the sample resulting from the source and sink at the edges, we used a model transparent alloy, namely the well-characterized succinonitrile-d-camphor (SCN-DC) alloy in a dilute-concentration range, in semi-thin samples. In such a confined-3D geometry, deep cells with a three-dimensional (3D) shape arrange within a single row. This permits real-time observation of the evolution of the solid-liquid interface with a standard optical microscope. Quantitative numerical simulations using the physical parameters of dilute SCN-DC alloys were carried out using a well-developed quantitative PF model of dilute binary alloy DS[23,24,34,35]. Systematic numerical results were obtained by varying V in a deep-cell regime, and the misorientation angle α_0 between 5° and 20°.

Both experiments and numerical simulations show that, after a long transient, the cell source at the divergent GB operates regularly. As a result, the total number of cells in the sample remains constant and the spacing reaches a steady-state spatial distribution where λ is uniform and much larger than λ_{min} in most of the sample, and drops abruptly to a small value $\sim \lambda_{min}$ inside a boundary layer near the convergent GB. This steady-state distribution is established by the lateral propagation of a front separating regions of larger and smaller spacings from the divergent GB towards the convergent GB. Importantly, this propagation takes place on a much longer time scale than the competitive growth transient at the start of an experiment during which cell elimination establishes the initial spacing distribution inside the sample with a spacing slightly larger than λ_{min}[15,16,20–22,25]. Consequently, propagative spacing selection can be investigated separately from the establishment of the initial spacing distribution. This initial distribution is not studied in detail here since, on the long time scale of the present experiments and simulations, it is completely "erased" by the propagative source-sink selection mechanism that establishes an entirely different spatial distribution of larger λ.

We propose a simplified geometrical model that can be numerically studied to predict the long-time spatiotemporal evolution of the array spacing. In addition, we derive a nonlinear advection equation that describes the evolution of the spacing distribution in a continuum limit and can be used to predict analytically the invasion velocity of the large spacing region inside the sample using

only the relationship between local growth orientation and local spacing (α/α_0 vs. Pe) as input into the theory. Those models yield predictions in excellent quantitative agreement with numerical and experimental results. Moreover, they show that the spacing modulations, which are initially present or possibly provoked during the course of a long-time DS run by any experimental imperfection, are advected in the same direction as the cell drifts at a rate that is noticeably smaller than $V_d \equiv V \tan\alpha$, and eventually eliminated at the convergent GB.

The numerical and experimental methods are described in Section II A. We propose an overview of the main results in Section III A, and some useful details about the relationship between the growth orientation of tilted cells and the local spacing in reference to previous works in Section III B. Simple models for analyzing the (primary) spacing evolution are presented in Section III C. Numerical and experimental results are presented, analyzed and discussed in Sections III D and III E, respectively. Conclusions are presented in the last section.

II. METHODS

A. Phase-field model

We used a recent 3D phase-field (PF) model that describes the solidification dynamics of a single-phase alloy in a one-sided limit (no diffusion in the solid)[19,20,32,36–38]. This model includes the so-called anti-trapping current that has been previously introduced in PF models to quantitatively predict the interface dynamics during solidification experiments of dilute binary alloys[37,38]. We also replaced the classical phase field φ ($\varphi = +1$ in the solid and -1 in the liquid) with the preconditioned phase field ψ defined by $\varphi \equiv \tanh(\psi/\sqrt{2})$, thus permitting to enhance the numerical stability of the PF simulations with large grid spacings[39]. We used a GPU (Graphic Processing Unit) architecture to improve the computational performance[21,23,30,40].

In order to produce a tilted-cell array in the 3D PF model, the misorientation angle α_0 is introduced into the surface tension anisotropy as described in Refs.[30,40]. Then, the angles α_0 and α (Fig. 1) are measured from the $\mathbf{x}$ axis that is parallel to the temperature gradient G. The detailed equations for the ψ field including a misorientation angle and dimensionless solute concentration U can be found elsewhere[30,40]. We implemented the thermophysical data of a SCN-0.24wt% camphor alloy[23,24,35,41–43], which are listed in Table I along with numerical parameters for the PF model. This model used a frozen-temperature approximation, and the temperature gradient was set to $G = 12\ \mathrm{K\,cm^{-1}}$.

We performed PF simulations using three different values of the solidification velocity, $V = 4, 12$, and $20\ \mu\mathrm{m\,s^{-1}}$ for different interface thicknesses $W/d_0 \approx 47.56$, 28.26, and 17.23, respectively, where $d_0 = \Gamma/(|m|c_\infty(1/k - 1))$ is the chemical capillary length with the Gibbs-Thomson coefficient Γ and the nominal composition $c_\infty = 0.24$wt%. Then, the grid spacing Δx and the Euler explicit time step Δt are chosen as $\Delta x \approx 3.00$, 1.78, and 1.09 μm, and $\Delta t \approx 5.00 \times 10^{-3}$, 1.75×10^{-3}, and 6.55×10^{-4} s in order of increasing V (see Table I).

For a thin-sample geometry, sample sizes were set to $L_x \times L_y \times L_z = 1290 \times 2490 \times 114\ \mu\mathrm{m}^3$ for $V = 4\ \mu\mathrm{m\,s^{-1}}$, $709 \times 2563 \times 82\ \mu\mathrm{m}^3$ for $V = 12\ \mu\mathrm{m\,s^{-1}}$, and $485 \times 1998 \times 50\ \mu\mathrm{m}^3$ for $V = 20\ \mu\mathrm{m\,s^{-1}}$, where L_x, L_y, and L_z correspond to the domain size along the $\mathbf{x}$, $\mathbf{y}$, and $\mathbf{z}$ axes, respectively. In all situations, the sample width L_y was large enough to form more than ten cells in steady-state (with the exception of the periodic-array simulations presented at the beginning of Section III B). Thermal fluctuations were introduced by adding a random noise with a strength $F_\psi = 0.01$ onto the ψ field[23,30,32,35,40]. No-flux (or reflection) boundary conditions were imposed at the lower/upper limits of the simulation domain ($x = 0$ and $x = L_x$), the immobile GBs ($y = 0$ and $y = L_y$), and the walls that delimit the sample along the $\mathbf{z}$ axis ($z = 0$ and $z = L_z$). We moreover imposed a finite-wetting condition at the $z = 0$ and $z = L_z$ boundaries with a slope $d\psi/dz|_{z=0} = -d\psi/dz|_{z=H} = +1$[21,32,40]. The long duration time of the simulations (20000 s for $V = 4\ \mu\mathrm{m\,s^{-1}}$; 2000 s for higher velocities) allowed us to simulate the dynamics of tilted-cell arrays over several centimeters. The cell-tip positions within a single row of cells were measured at the middle of the sample, i.e. in a $\mathbf{x}$-$\mathbf{y}$ plane located at $z = H/2$, where $H = L_z$ is the sample thickness, as illustrated in Fig. 2a. These measurements in turn were used to calculate the local spacing λ, the drift velocity V_d, and the cell-tilt angle α.

For calibration purposes, we also carried out PF simulations of a single cell in a channel with periodic boundary conditions in the $\mathbf{y}$ direction. This was used to measure V_d in a perfectly ordered array with a fixed spacing $\lambda = L_y$. For those simulations, we used an initial guess made of a pre-calculated axial cell ($\alpha_0 = 0°$) with $\lambda =$ 114, 82, and 50 μm for $V = 4$, 12, and 20 $\mu\mathrm{m\,s^{-1}}$, respectively, in a squared-section simulation box (i.e. $L_y = L_z$). Then, we re-started a simulation using the axial cell by implementing a finite misorientation angle α_0. The λ value was changed by adding (or subtracting) a grid-spacing unit Δx to the width L_y of the sample, and using a bilinear interpolation from the previous steady-state simulation.

B. Experiments

A SCN-0.3 ± 0.05mol% DC alloy was prepared with purified SCN (distillation) and DC (sublimation). Alloy samples were enclosed in thin containers made of two flat glass plates glued to each other, and separated by polymer spacers of thickness $H = 100\ \mu$m. The sample

TABLE I. Material, control, and numerical parameters. Thermophysical parameters of SCN alloys are taken from Refs.[23,35,41–44,46,47]. For the PF simulations, we used a fixed $W/\Delta x = 1.2$ and other numerical parameters depend on V. * Experimental parameters ($V = 4\ \mu\mathrm{m\,s^{-1}}$); see Section III E.

Parameter	Symbol	Value	Unit
Solute concentration	c_∞	0.24	wt% camphor
		$0.3 \pm 0.05^*$	mol% d-camphor
Temperature gradient	G	12	$\mathrm{K\,cm^{-1}}$
		$75 \pm 5^*$	
misorientation angle	α_0	5, 10, 15, 20	degrees (°)
		$15.5 \pm 0.5^*$	
Pulling velocity	V	4, 12, 20	$\mu\mathrm{m\,s^{-1}}$
Diffusion coefficient	D	270	$\mu\mathrm{m^2 s^{-1}}$
Liquidus slope	m	-1.365	$\mathrm{K\,wt\%^{-1}}$
Partition coefficient	k	0.21	-
Gibbs-Thomson coefficient	Γ	6.478×10^{-8}	K m
Anisotropy strength	ε_4	0.011	-
Interface thickness	W	47.56, 28.26, 17.23	d_0
Grid spacing	Δx	3.00, 1.78, 1.09	μm
Time step	Δt	5.00×10^{-3}, 1.75×10^{-3}, 6.55×10^{-4}	s

length (along the **x** axis) was of about 64 mm, and the width L_y (along the **y** axis) of 2.8 ± 0.2 mm (this typically corresponds to 20 cells). Solidification experiments were carried out over a total length of 30 to 40 mm, beyond which substantial macrosegregation effects were observed. Previous to DS, the samples were filled by capillarity with the melted alloy under a low-pressure argon atmosphere, and then rapidly cooled down to room temperature. During this process, multiple nucleation sites were activated, thus resulting in the formation of a polycrystal.

The DS apparatus was made of two temperature-regulated copper blocks, separated from each other by a distance of 5 mm (for details, see Ref.[44] and references therein). A fixed temperature gradient $G = 75 \pm 5\ \mathrm{K\,cm^{-1}}$ established by heat conduction in the sample along the **x** axis. Solidification was performed by translating the sample along the **x** axis at a velocity $V = 4\ \mu\mathrm{m\,s^{-1}}$ with a DC motor. The whole setup was installed on the stage of a standard optical microscope. The solid-liquid interface was visualized (transmitted light) in real time over the entire width of the sample with a numerical camera connected to a PC for image storage and analysis.

At the beginning of the experiment, the alloy was partially melted directionally down to a crystal selector placed on the cold end of the sample[45]. A single, randomly oriented crystal was then grown and expanded along a funnel-shaped region until it occupied the whole width of the sample. The orientation of the crystal was measured, within a 1° error margin, by growing fully developed dendrites at a large velocity ($V > 200\ \mu\mathrm{m\,s^{-1}}$). The operation was repeated until an "in-plane" crystal such that a [100] axis (the preferred dendrite growth axis in SCN-based alloys at low growth rate) belonged to the sample **x**-**y** plane was selected.

III. RESULTS AND DISCUSSION

A. Overview

In both PF simulations and experiments, regular solidification runs were started (time $t = 0$ s) after a planar solid-liquid interface was equilibrated at rest ($V = 0\ \mu\mathrm{m\,s^{-1}}$). Small cells were observed to appear during the initial solute-redistribution transient after the velocity of the planar interface becomes larger than the threshold velocity V_c[4,15,16]. Their spacing was systematically and substantially smaller than the lower stability limit of steady periodic cells at the imposed velocity. This entailed an initial coarsening dynamics by progressive elimination of a large proportion (about one out of two) of the initial cells, which lasted until a one-row pattern of confined-3D cells with a stable average spacing was formed. Three key features must be noted at this stage: (i) after the very last cell-elimination event in the middle of the sample, the cellular pattern presented a nonuniform spatial spacing distribution $\lambda(y)$; (ii) tilted cells drift away from the divergent GB, which thus acts as a source of new cells via a tertiary branching process; (iii) cells are eliminated in the vicinity of the convergent GB. The aim of the present study is to characterize and model the long-time behavior of tilted-cell patterns by taking those three elements –nonuniform initial spacing distribution, cell source at the divergent GB, and cell sink

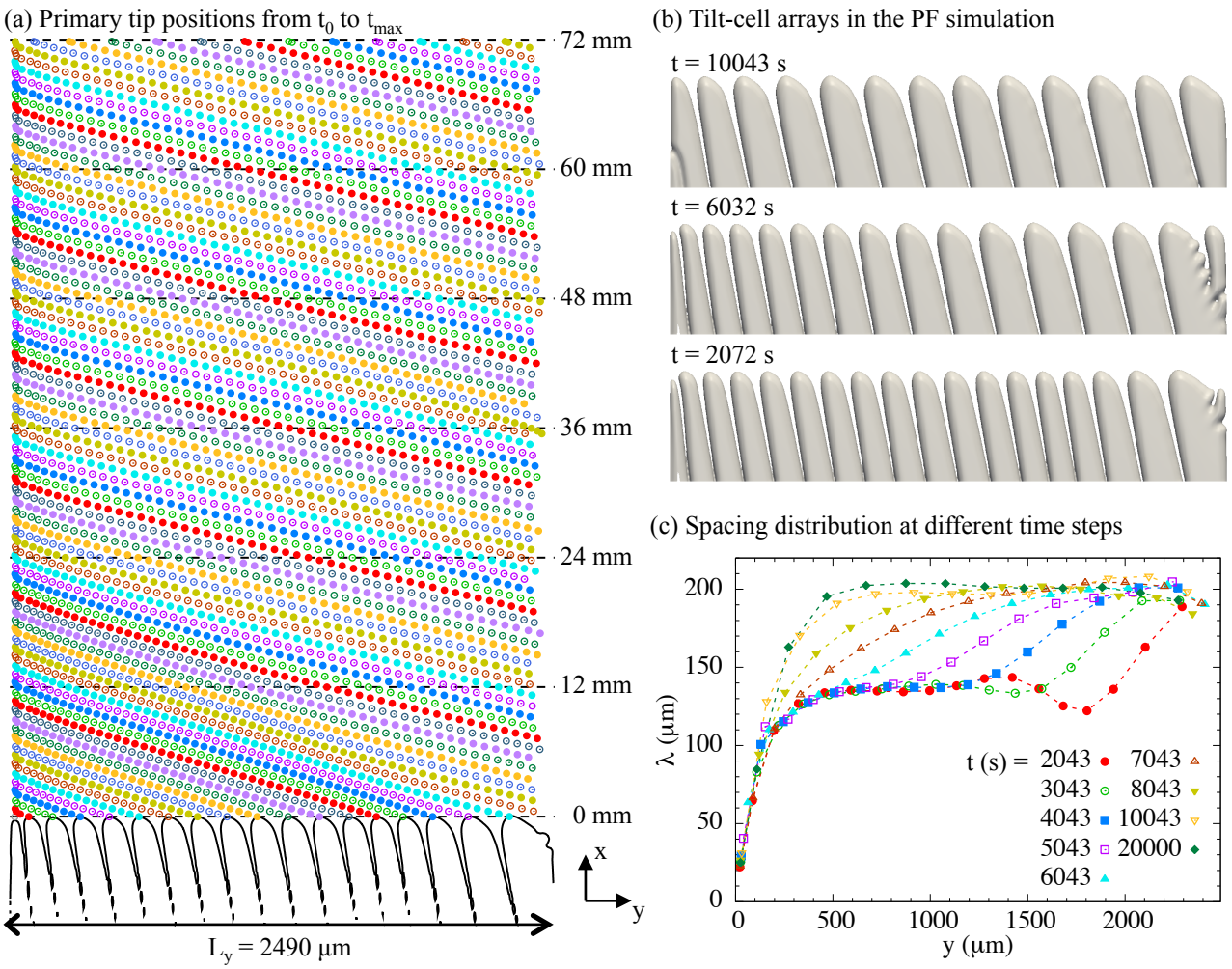

FIG. 2. Numerical simulation of a tilted-cell array in a SCN-0.24wt% camphor alloy ($\alpha_0 = 15°$; $V = 4\ \mu\mathrm{m\,s^{-1}}$; $G = 12\ \mathrm{K\,cm^{-1}}$). (a) Simplified spatiotemporal diagram: cell tip positions (circles) at regular time intervals (≈ 63 s) from t_0 to the end of the simulation at $t_{max} = 20000$ s. Dashed horizontal lines and numbers are related to the solidified length $V(t - t_0)$. Bottom: profile of the cross-section of the solid-liquid interface in the median plane of the sample ($z = H/2$) at time t_0. (b) Tilted-cell arrays at times $t = 2072$ s, 6032 s, and 10043 s (bottom to top) of the same simulation as in (a). (c) Spatial distribution of the primary spacing $\lambda(y)$ for 9 successive times corresponded to different symbols. Dotted lines are guides to the eye (color online).

at the convergent GB– into account.

Let us go into more quantitative details. Simulations were run for a time t ranging from $t = 0$ at which the sample starts to be pulled at constant velocity to $t = t_{max}$. We denote by t_0 the time at which the initial cell elimination coarsening process was completed (this time has no need to be defined with a better accuracy than, say, $\pm\lambda/2V$). In typical PF simulations, we measured $t_0 \approx 4040$ s for $\alpha_0 = 5°$ (but 2040 s for higher α_0 values) at $V = 4\ \mu\mathrm{m\,s^{-1}}$, 900 s for $V = 12\ \mu\mathrm{m\,s^{-1}}$, and 220 s for $V = 20\ \mu\mathrm{m\,s^{-1}}$. This represents a long-duration process as compared to the reference diffusion time $\tau_d = D/V^2$. Values of t_{max} for the different simulations were $t_{max} = 20000$ s ($t_{max}/t_0 \approx 5$ and 10) for $V = 4\ \mu\mathrm{m\,s^{-1}}$ and $t_{max} = 2000$ s for both $V = 12\ \mu\mathrm{m\,s^{-1}}$ ($t_{max}/t_0 \approx 2$) and $V = 20\ \mu\mathrm{m\,s^{-1}}$ ($t_{max}/t_0 \approx 9$). In comparison, t_{max} was close to $2t_0$ in the experiments. Therefore, the long-time dynamics after t_0 was fully disconnected from both the initial solute redistribution transient, and cell-spacing rearrangement processes.

In the simplified spatiotemporal diagram of Fig. 2a (PF simulation), the drifting motion of the cells (circles) is made clearly visible. Symbols of different colors correspond to different cells. Horizontal rows are isochrones. While the cells grow (the main solidification axis **x** is vertical), they drift laterally from the divergent GB (on the right-hand side) towards the convergent GB (on the left-hand side). Symbols of different colors therefore alternate at the boundaries, which corresponds to the appearance of new cells by tertiary branching at the divergent GB (this is illustrated in Fig. 2b), and cell elimination at the convergent GB. Most of the time, this process op-

erates quite regularly, as shown in Fig. 2a. A similar sink-and-source dynamics is observed in the experiments.

We measured the spacing distribution $\lambda(y)$ at different time steps (Fig. 2c). In the middle of the initial pattern at t_0, the spacing was slightly modulated about an average value of, here, about 130 μm and exhibited a steep variation close to the convergent and divergent GBs. During the solidification run, the spacing value λ_M delivered from the source propagated across the sample. At the end of the process, the spacing distribution reached a steady-state characterized by a large plateau, signalling the extension of a periodic pattern from the divergent GB over the major part of the sample width, and a steep drop in a region close to the convergent GB. The value of λ_M was larger than the average spacing at time t_0. The latter feature was systematically observed in our PF simulations. It is also compatible with previous reports of a progressive increase of the average primary spacing over long timescales during DS experiments[14,48–52].

This qualitative description of the tilted-cell pattern dynamics opens to further questions, among which that of the rate of the advection (vs. smoothing out) of incipient (or accidental) modulations.

B. Dependence of the cell-tilt angle on the local spacing in modulated patterns

For reference purposes, we measured the dependence of the cell-tilt angle α on the Péclet number in periodic arrays for the SCN-DC alloy under consideration. We performed PF simulations with periodic boundary conditions, for various values of V ($= 4, 12$, and 20 μm s^{-1}), α_0 ($= 5, 10, 15$ and 20°), and L_y ($= \lambda$). We let λ increase to the upper limit λ_{max} at which a tertiary branching instability occurs[20], and decrease to the lower limit λ_{low} (Table II). Below the lower limit of a spacing, a cell has a planar interface perpendicular to the temperature gradient axis like a 2D ribbon shape[19].

When a cell travels laterally, its drift velocity V_d was calculated as

$$V_d = \left| \frac{\mathrm{d}y_t}{\mathrm{d}t} \right| , \qquad (1)$$

where y_t was the position of the cell tip along the $\mathbf{y}$ axis, and t was the time. Then, the tilt angle α was calculated by using the geometrical relation

$$\tan\alpha = V_d/V . \qquad (2)$$

The α/α_0 data are shown as red full squares in the graphs of Fig. 3 and can be used to define the function $\alpha = \alpha_0 F(\mathrm{Pe})$ in Eq. (3), which is related to the misorientation angle α_0 and the local adimensionalized spacing $\mathrm{Pe} = \lambda V/D$.

We also measured local V_d and λ values in the modulated tilted-cell patterns observed during large-scale PF simulations. Each data set cumulates measurements performed approximately every 63 s, 8 s, and 3 s for $V = 4, 12$, and 20 μm s^{-1}, respectively, starting from the above defined time t_0 to the end of the simulations t_{max}. We systematically discarded the sidebranching and sinking cells located close to the GBs. The obtained α/α_0 data are reported as blue empty circles in the graphs of Fig. 3 along with the periodic-array measurements. The two kinds of data are obviously close to each other. The modulated-pattern data exhibit a substantial dispersion, but it is worth noting that the most departing points were measured in regions with steep $\lambda(y)$ variations near the GBs.

We finally recall that the following law:

$$\frac{\alpha}{\alpha_0} \equiv F(\mathrm{Pe}) = 1 - \frac{1}{1 + f\,\mathrm{Pe}^g} , \qquad (3)$$

where f and g are alloy-dependent constants, has been previously proposed for a general, yet empirical description of the $F(\mathrm{Pe})$ function[28–33]. Best-fit adjustments of that law with our periodic-array data points are shown in the graphs of Figs. 3a-f. The corresponding constants f and g are listed in Table II. Two comments are in order. First, the parameters f and g at a fixed α_0 (see the data for $\alpha_0 = 15°$ in Table II) vary when V is changed. In other words, PF simulations of confined-3D patterns show that the parameters can change when $V > 15V_c$, where the critical velocity $V_c = DG/\Delta T_0$ with $\Delta T_0 = mc_\infty(1/k - 1)$, as observed in the 2D patterns[33]. On the other hand, the $\alpha/\alpha_0 = F(\mathrm{Pe})$ function exhibits the same "universality" for 2D arrays at $V < 15V_c$[28]. Second, the best-fitting curves agree relatively well with the PF simulations, but not perfectly. Considering that not only the $F(\mathrm{Pe})$ function, but also the derivative of that function will be used later on in this paper for a quantitative analysis of the spatiotemporal dynamics of tilted-cell arrays, we think that using the (interpolated) results of the PF simulations in the models presented in the next section is more reliable than using the approximate law of Eq. (3).

TABLE II. Control parameters (pulling velocity V and misorientation angle α_0) of PF simulations using periodic tilted-cell arrays. λ_{low} (λ_{max}): lower (upper) limit of the spacing interval. f and g: fitting parameters in Eq. (3). The fitting curves are shown in Fig. 3 as black lines.

V (μms^{-1})	α_0 (°)	λ_{low} (μm)	λ_{max} (μm)	f (-)	g (-)
4	5	22.5	301.5	0.433	2.118
	10	22.5	313.5	0.416	2.114
	15	22.5	322.5	0.389	2.108
	20	22.5	337.5	0.356	2.101
12	15	16.9	220.2	0.165	2.226
20	15	10.3	190.8	0.094	2.557

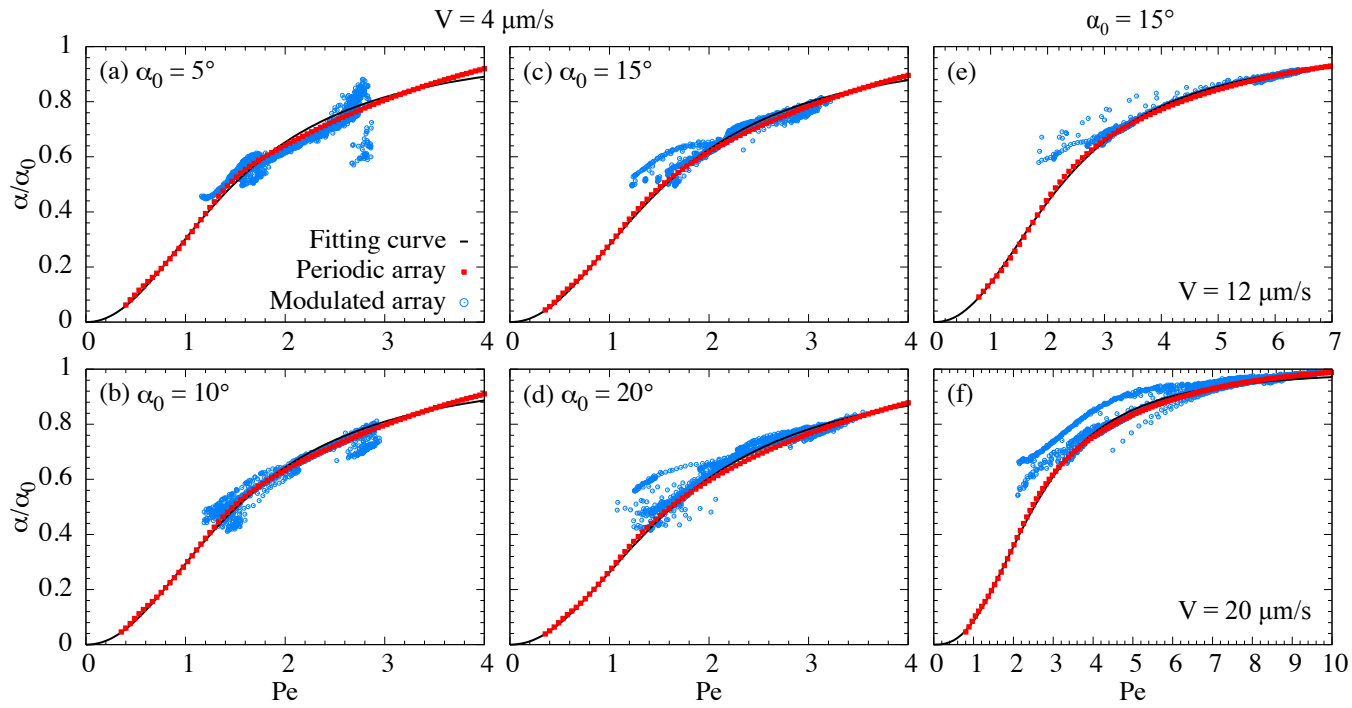

FIG. 3. Ratio α/α_0 between the cell-tilt angle an the misorientation angle as a function of the Péclet number Pe, measured from PF simulations for different α_0 and V values. Red full squares and black solid lines: periodic arrays, and best-fitting curves using Eq. (3) (also see Table II), respectively. Blue empty circles: modulated arrays (see text).

C. Theoretical models of propagative spacing selection

We insert here the definition of the two models that we use for the analysis of our numerical and experimental data presented in the next section.

1. *Geometrical model*

We propose a simple "geometrical" model based on a discrete treatment of the lateral motion of individual cells to describe the spatiotemporal evolution of the spacing of tilted-cell patterns. We make the reasonable assumption that the growth orientation of a tilted cell within an array with a slowly varying spatial modulation of spacing is described locally by the $\alpha/\alpha_0 = F(\mathrm{Pe})$ function determined for a periodic array (red squares in Fig. 3). This assumption yields the evolution equation

$$\frac{dy_i}{dt} = -V_d = -V \tan\left[\alpha_0 F\left(\frac{y_i - y_{i+1}}{D/V}\right)\right], \qquad (4)$$

for the lateral coordinate y_i of the tip of the i^{th} cell shown schematically in Fig. 4, where the local spacing between two cell tips is taken equal to $y_i - y_{i+1}$ (with the positive y axis pointing to the right and the cell index i increasing from right to left). We note that, in the framework of this simple phenomenological model, the local spacing influencing the growth orientation of the i^{th} could be chosen as well as $y_{i-1} - y_i$ or any weighted sum $p(y_i - y_{i+1}) + (1-p)(y_{i-1} - y_i)$, with p varying from 0 to 1, of the spacings defined with the two neighboring cell tips. We investigated different values of p and empirically found that $p = 1$ gave the best predictions. This finding suggests, as previously announced by J. Deschamps[54], that the lateral velocity of a cell in the array is more strongly influenced by the spacing with its front neighbor, towards which it is traveling, than its rear neighbor. This assertion is moreover supported by the finding in

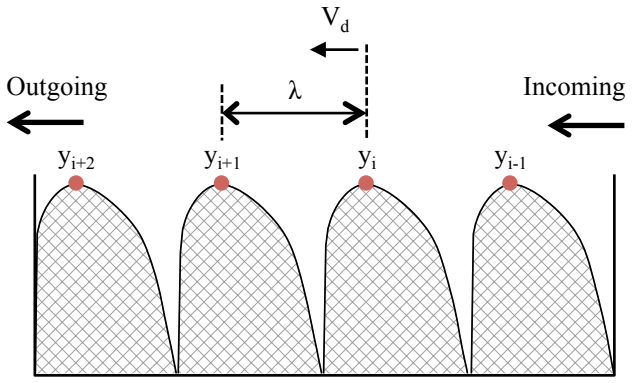

FIG. 4. Schematic tilted-cell array far away from any GB. λ: primary spacing. V_d: lateral drift velocity. Red circles: cell tips. Within such a region of the pattern, the cell density is conserved.

Ref.[33] that the asymmetry of the shape of a tilted cell is typically strong on the side of the preceding neighbor cell (here, cell i+1), whereas it is much less pronounced on the side of the following cell (here, cell i-1). In all numerical solutions of the geometrical model presented here, we will therefore use the value $p = 1$. This geometrical model quantitatively predicts the spacing evolution of tilted cells away from the convergent and divergent GBs observed in experiments[54].

In order to account for the source-sink dynamics at the two GBs, we create a new cell with a spacing λ_M when the distance of the tip of the right-most cell closest to the divergent GB (right edge of the sample) exceeds λ_M (source), and we remove the left-most cell when its distance to the convergent GB (left edge of the sample) becomes smaller than λ_e. Eq. (4) defines a set of coupled ordinary different equations for the time-evolution of cell tips that are solved using an Euler explicit time stepping scheme with a time step $\Delta t = 0.1$ s for the experiments and simulations. The above conditions for cell creation and removal are checked at each time step.

2. *Nonlinear advection equation*

To complement the discrete geometrical model, we derive an equation for the slow spatiotemporal evolution of λ treated as a continuous function of the lateral position y. This equation can be readily obtained from the conservation of the total number of cells in the array away from the edges where cells can be created or eliminated. For this, we define the cell density (number of cell per unit length of the array) $\rho \equiv \lambda^{-1}$. The cell density obeys the continuity equation

$$\partial_t \rho - \partial_y \left[V_d \cdot \rho \right] = 0 \,. \tag{5}$$

This equation is simply the statement that, in the absence of cell creation or elimination, the change of the total number cells in a segment of the array away from the sample edges (Fig. 4), which is much larger than the cell spacing but much smaller than the characteristic scale of variation of λ, must be equal to the difference of flux of cells entering or leaving through the left and right boundaries of this segment. Note that the minus sign of the second term in the continuity equation originates from the fact that the local drift velocity of cells towards the left is defined positively ($V_d \geq 0$) while the positive y axis points towards the right. Substituting $\rho = 1/\lambda$ in Eq. (5), we obtain the advection equation for λ

$$\partial_t \lambda = V_\lambda \partial_y \lambda \,, \tag{6}$$

where we have defined

$$V_\lambda \equiv V_d - \lambda \frac{\mathrm{d}V_d}{\mathrm{d}\lambda} \,. \tag{7}$$

This equation is nonlinear because, as before, V_d is a nonlinear function of λ defined by $V_d = V \tan\alpha = V \tan(\alpha_0 F(\mathrm{Pe}))$ where the local growth orientation $\alpha = \alpha_0 F(\mathrm{Pe})$ and hence the drift velocity V_d is assumed to be a function of the local spacing. Even though the group velocity in Eq. (7) can become negative for small enough spacing, the critical spacing below which the group velocity becomes negative is very close to the smallest stable spacing. As a result, dynamically selected spacings in the present simulations and experiments fall in a range of spacing for which the group velocity is positive. Note that, using the standard relations between a frequency $\omega \equiv V_d k_\omega$ and a wave number $k_\omega = 2\pi/\lambda$ of traveling waves, V_λ defined by Eq. (7) can also be written in form of a group velocity $V_\lambda = \mathrm{d}\omega/\mathrm{d}k_\omega$.

Eq. (6) is reminiscent of Burgers' equation[53], which is well-known to form shocks. In contrast, in the simulations shown in Fig. 2c, the front separating regions of larger and smaller spacing propagates at a nearly constant velocity without becoming steeper, as would be expected if shock formation was present. The shock-less behavior can be related the fact that the drift velocity is predominantly a linear function of λ in the front region. Hence, the drift velocity can be expanded in the form

$$V_d(\lambda) = V_d(\lambda_p) + \left[\frac{\mathrm{d}V_d}{\mathrm{d}\lambda} \right]_{\lambda=\lambda_p} (\lambda - \lambda_p) + \ldots \tag{8}$$

up to small $\mathcal{O}((\lambda - \lambda_p)^2)$ corrections, where λ_p is defined as the "median spacing", which is the characteristic value of λ in the propagating front region. It is arbitrarily defined here as the value of λ that is half way between the smaller and larger values of λ in regions ahead and behind the front, respectively, where λ is spatially uniform. Indeed, values of α (blue circles in Fig. 3), and hence the drift velocity $V_d = V \tan\alpha \approx V\alpha$ for small α, are to a good approximation of a linear function using the dimensionless spacing. Substituting the approximation Eq. (8) into Eq. (7) yields the prediction

$$V_\lambda \approx V_d(\lambda_p) - \left[\frac{\mathrm{d}V_d}{\mathrm{d}\lambda} \right]_{\lambda=\lambda_p} \lambda_p \,. \tag{9}$$

There are two implications of this result. First, the advection velocity is approximately constant in the entire front separating large and small spacings regions, such that the front simply propagates in a shape-preserving manner with a velocity V_λ without forming shocks. Second, since the slope of the drift velocity-spacing relation is positive ($[\mathrm{d}V_d/\mathrm{d}\lambda]_{\lambda=\lambda_p} > 0$), the front propagation velocity V_λ is typically several fold smaller than the local drift velocity $V_d(\lambda_p)$ in the front region. In fact V_λ defined by Eq. (9) is the $\lambda = 0$ intercept of a straight line fit of the $V_d(\lambda)$ curve and this intercept must always be smaller than $V_d(\lambda_p)$. We use Eq. (9) to predict the front propagation velocity in simulations and experiments. For the simulations, we compute V_d and its slope using the growth orientation vs. spacing relation $\alpha/\alpha_0 = F(\mathrm{Pe})$ determined from simulations with periodic arrays of different spacing (red full squares in Fig. 3) and λ_p extracted from simulations. We have also computed V_λ as

the $\lambda = 0$ intercept of a straight line fit of the α/α_0 vs. Pe values measured on the propagating front during simulations (blue empty circles in Fig. 3), and found that the two methods predict values of V_λ within 15% of each other. We only report in this paper values of V_λ computed with the first method for the simulations. For the experiments, the slope $\mathrm{d}V_d/\mathrm{d}\lambda$ is estimated by a best-fit line of Eq. (3) that is fit to the experimental measurements (empty blue diamonds in Fig. 10b), then we compute V_λ at λ_p. The $\lambda = 0$ intercept of a straight line fit of the α/α_0 vs. Pe values measured on the propagating front during experiments is also close to the computed V_λ.

The nonlinear advection equation, i.e. Eq. (6), neglects the effect of "phase diffusion", which generically relaxes spatially modulated nonequilibrium patterns towards a spatially uniform spacing[55]. This effect could be incorporated by the addition of a diffusion term $D_\lambda \partial^2\lambda/\partial y^2$ on the right-hand-side of Eq. (6). While "phase diffusion" has been shown to strongly influence the stability of lamellar eutectic growth patterns[56,57], its effect on array patterns of deep cells and dendrites in the presence of crystalline anisotropy turns out to be much weaker. We explicitly computed D_λ by PF simulations of well-oriented ($\alpha_0 = 0$) arrays in which we analyzed the decay of slowly varying spatial modulations of the spacing and found D_λ to have a very small value ($D_\lambda \approx 20.1\ \mu\mathrm{m}^2\mathrm{s}^{-1}$), which would have a negligible effect on front propagation in the present PF simulations and experiments. The details to estimate D_λ are shown in Appendix A.

D. Comparison of phase-field simulations with theoretical models

We performed systematic PF simulations of confined-3D arrays of tilted cells by varying the misorientation angle α_0 and the solidification velocity V (also see Section III A and Fig. 2). Let us first focus on the effect of the misorientation angle. We considered four different α_0 values, namely, 5, 10, 15, and 20°, and kept the velocity $V = 4\ \mu\mathrm{m\,s}^{-1}$. The spatiotemporal evolution of the corresponding DS patterns is shown in the graphs of Fig. 5a. In each of those graphs, the measured $\lambda(y)$ (symbols) are plotted at successive simulation times from t_0 to t_{max}. For all considered α_0 values, the propagation of the spacing λ_M delivered from the source towards the inner-grain region is clearly visible. In the simulations, the selected spacings at the divergent GB are typically $\lambda_M \approx 180$, 192, 201, and 218 μm for $\alpha_0 = 5$, 10, 15, and 20°, respectively. As mentioned above, λ_M was systematically larger than the initial average spacing at t_0. Note that most simulations reached a steady-state regime, with a uniform λ_M plateau and a steep drop near the sink, except for the smaller misorientation angle $\alpha_0 = 5°$, that is obviously for a very slow lateral drift velocity.

We implemented the geometrical model (Section III C 1) by using, for each pair of V and α_0 data, the spacing profile at t_0 as an initial condition (red continuous line). We let cells move with an instantaneous local velocity V_d(Pe) that was linearly interpolated from the ordered array simulations of Fig. 3. We used the steady-state values of λ_M for the cell branching criterion close to the divergent GB, and manually set the cell elimination limit to $\lambda_e = 54\ \mu$m at the convergent GB for the $V = 4\ \mu\mathrm{m\,s}^{-1}$ simulations (gray shaded area on the right and left side, respectively, in the graphs of Fig. 5a). The calculated spacing profiles are shown in the form of continuous lines in Fig. 5a. They superimpose remarkably well with the simulation results, in consideration of the simplicity of the geometrical model, and bring a clear evidence to the general dynamical scheme that can be summarized as follows: advection and elimination of the initial modulations, formation of a propagation front of a $\lambda = \lambda_M$ plateau, and convergence towards a steady-state profile.

There are slight discrepancies between the geometrical model and the PF simulations, which can be essentially classified according to two separate features. First, the shape of the steep-drop region close to the convergent GB is not fully reproduced. This is in agreement with our observation (Section III B) that the local cell-drift dynamics may severely depart from the V_d(Pe) law of an ordered-array if the spacing gradients are large. Second, the prediction by the geometrical model is apparently less reliable for $\alpha_0 = 5°$. We can advance that a phase-diffusion process can predominate for a vanishing misorientation and induce spreading of the propagation front that cannot be fairly reproduced by the geometrical model.

We tested the prediction using a group velocity, i.e. V_λ in Eq. (7) (see Section III C 2). For each PF simulation, we defined a median spacing λ_p between the initial average spacing at t_0 (close to the lower plateau of a λ distribution) and λ_M (Table III). The position of the spacing λ_p propagates from an initial position y_0 at t_0 towards the sink, as schematically indicated by the black arrows in Fig. 5a. We followed this propagation as a function of time by linearly interpolating the positions y_p that correspond to λ_p in the $\lambda(y)$ profiles at different

TABLE III. Calculated V_d and V_λ at the median spacings λ_p in confined-3D array simulations.

V ($\mu\mathrm{m\,s}^{-1}$)	α_0 (°)	λ_p (μm)	V_d ($\mu\mathrm{m\,s}^{-1}$)	V_λ ($\mu\mathrm{m\,s}^{-1}$)
4	5	145	0.2339	0.0955
	10	145	0.4641	0.1828
	15	165	0.7419	0.2958
	20	165	0.9691	0.3466
12	15	105	2.6261	1.5786
20	15	85	4.8155	3.3664
	15	105	5.0832	3.9957

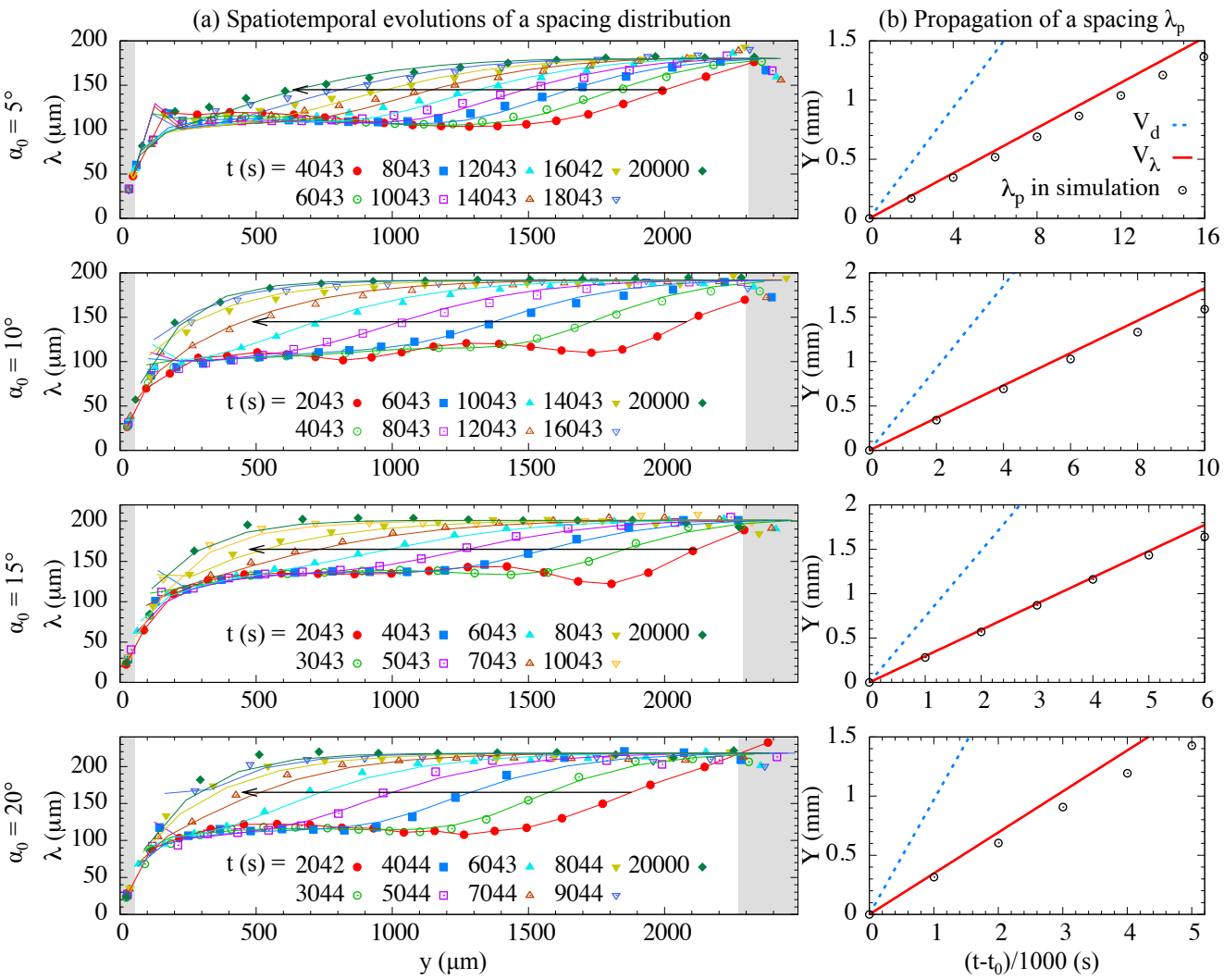

FIG. 5. Spatiotemporal evolution of the primary spacing λ and spacing-propagation dynamics for $\alpha_0 = 5°$ (first row), $10°$ (second row), $15°$ (third row), and $20°$ (fourth row) at $V = 4\ \mu\mathrm{m\,s^{-1}}$ (PF simulations). In the graphs of (a), we reported the spacing profiles measured from the simulations (symbols), and calculated (solid lines) using the geometrical model (Section III C 1), with the PF distribution at time t_0 as a initial condition. Different symbols (and color online) are corresponded to different times. Right (left) gray shaded areas: location of the source (sink) in the model. Arrows are used to schematically trace the position y_p of the median spacing λ_p. In the graphs of (b), we reported the abscissa y_p corresponding to $\lambda = \lambda_p$ in the corresponding graphs of (a) as a function of time $t - t_0$, using, for convenience, $\mathrm{Y} = |y_p - y_0| = 0$ for $t = t_0$ (circles). Slopes of the straight lines correspond to V_λ (solid lines) and V_d (dashed lines). See text for definitions.

times. We reported the quantity $\mathrm{Y} = |y_p - y_0|$ as a function of $t - t_0$ in the graphs of Fig. 5b. It appears clearly that the propagation is essentially linear, and that the spacing propagation velocity, i.e. the slope of a linear fit of the $\mathrm{Y}(t - t_0)$ data (black empty circles), compares well with the group velocity V_λ calculated with Eq. (7), i.e. the slope of the red continuous lines. It can also be seen that V_d (the slope of the blue dashed lines) is much larger than both V_λ and the $\mathrm{Y}(t - t_0)$ slope. The calculated V_d and V_λ at a given spacing λ_p for α_0 are listed in Table III. It is worth mentioning that the calculated V_λ in Table III is always close to the intercept of a linearized $V_d(\lambda)$ (Section III C 2).

We also performed PF simulations at higher V (12 and 20 $\mu\mathrm{m\,s^{-1}}$), and kept $\alpha_0 = 15°$ as a constant (Fig. 6a). As in the above cases, λ_M is substantially larger than the initial average spacing, and it propagates from the source. In addition, a steady-state spacing profile is reached with a large uniform λ_M plateau. The region of the spacing drop near the sink is narrower as V increases. The quantitative agreement between the geometrical model and the PF simulations also seems all the better as V increases.

We again measured the position of the median spacing λ_p (105 μm for $V = 12\ \mu\mathrm{m\,s^{-1}}$; 85 μm for $V = 20\ \mu\mathrm{m\,s^{-1}}$; see black arrows in Fig. 6a) as a function of time. The

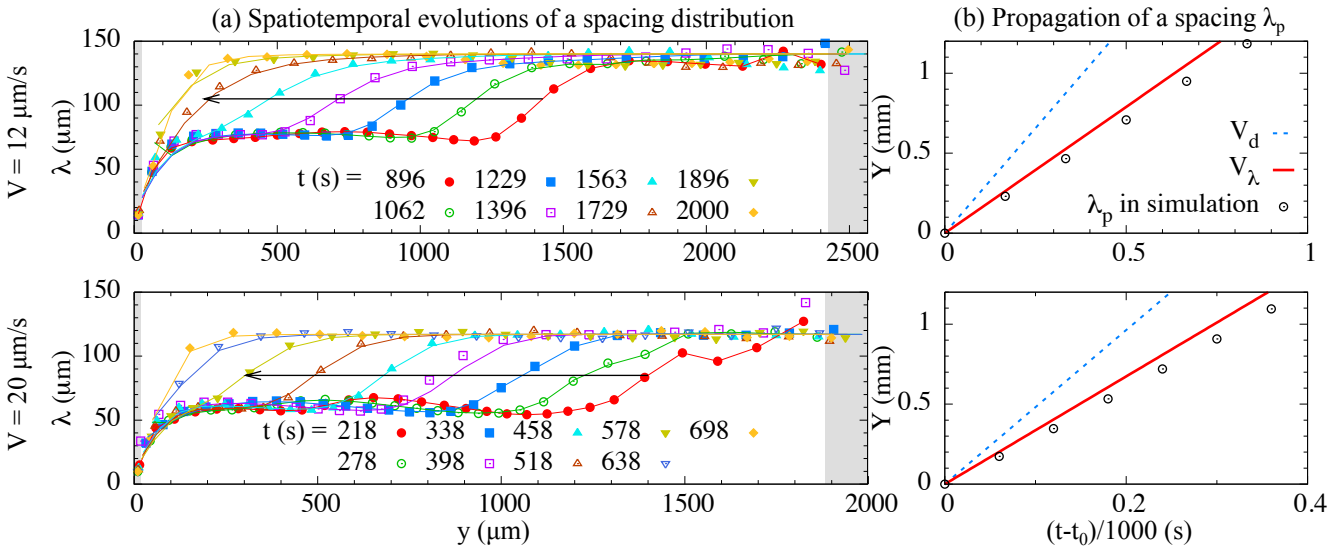

FIG. 6. Spatiotemporal evolution of the primary spacing λ (a) and spacing-propagation dynamics (b) for $V = 12\ \mu\mathrm{m\,s^{-1}}$ (first row) and $20\ \mu\mathrm{m\,s^{-1}}$ (second row) for $\alpha_0 = 15°$. Same representations as in Fig. 5. The spacing limits for the geometrical model are $(\lambda_M,\ \lambda_e) = (140\ \mu\mathrm{m},\ 27\ \mu\mathrm{m})$ for $V = 12\ \mu\mathrm{m\,s^{-1}}$ and $(117\ \mu\mathrm{m},\ 19\ \mu\mathrm{m})$ for $V = 20\ \mu\mathrm{m\,s^{-1}}$. Color online.

results are shown in Fig. 6b. Here as well, the spacing propagation is well predicted by the group velocity V_λ –and not by V_d (Table III).

In practice, the value of V_λ (for the chosen λ_p values) and the ratio V_λ/V_d increases as V increases (Fig. 7). If one refers to the relation $F(\mathrm{Pe})$ for $\alpha_0 = 15°$ (Fig. 3), it should be noticed that $\alpha \approx \alpha_0$ is reached for lower Pe values when V increases. Then, the derivative term in Eq. (7) becomes negligible (because $\mathrm{d}V_d/\mathrm{d}\lambda \sim \mathrm{d}\alpha/\mathrm{d}\lambda$ vanishes), which leads to $V_\lambda \to V_d$. Accordingly, it is indeed expected that the propagation rate of the spacing approaches V_d ($V_\lambda/V_d \to 1$) when V increases.

In most PF simulations of tilted-cell patterns, a long-lived steady-state was observed after the λ_M plateau had formed. Overall, their main features were negligibly sensitive to the small-scale dynamics of the tertiary branching (amplification of and competition between sidebranches). However, an anomalous event at the source can entail a marked modification of the tilted-cell pattern on a large scale. In Fig. 8a, one can see the growth and the propagation of two cells with a spacing significantly smaller than λ_M. The initial pattern (bottom of Fig. 8a) was in a steady-state situation (similar to that corresponding to the final time in the graph of Fig. 6a for $\alpha_0 = 15°$ and $V = 20\ \mu\mathrm{m\,s^{-1}}$). The simultaneous growth of two incipient sidebranches close to the divergent GB, and their transformation into two individual small-spacing cells is clearly seen (Fig. 8a). This induces a persistent depression in the spacing profile, which both travels laterally and smoothes out (Fig. 8b). This anomalous event did not occur additionally during the simulation, and a steady-state configuration was recovered. Again, the geometrical model predicts this complex behavior quite well as illustrated in Fig. 8b. We also followed the propagation of the depression in the spacing profile (with $\lambda_p = 105\ \mu\mathrm{m}$). As shown in Fig. 8c, the corresponding Y data from $t_1 = 1358$ s closely align with the linear law of slope V_λ (see Table III). In the PF simulations, this complex behavior was only occurred at this condition, i.e. relatively large α_0 and V.

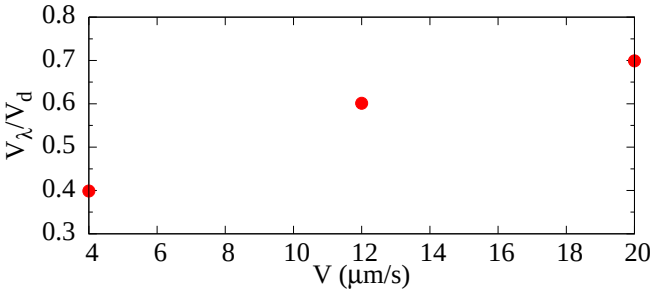

FIG. 7. Value of the ratio V_λ/V_d as a function of V.

E. Comparison of theoretical models and experiment

Fig. 9a shows a time series of snapshots of a tilted-cell array ($\alpha_0 = 15.5 \pm 0.5°$) during a DS experiment of the SCN-0.3mol% DC alloy. The image at $t_0 \approx 4000$ s is taken just after the last event of a series of cell eliminations (horizontal red line on the bottom of the spatiotemporal diagram of Fig. 9b), which occurred during the early stages of the experiment. On average, the primary spacing λ evolved from about 130 μm (before cell eliminations) to 180 μm (plateau region). The cell-tilt angle

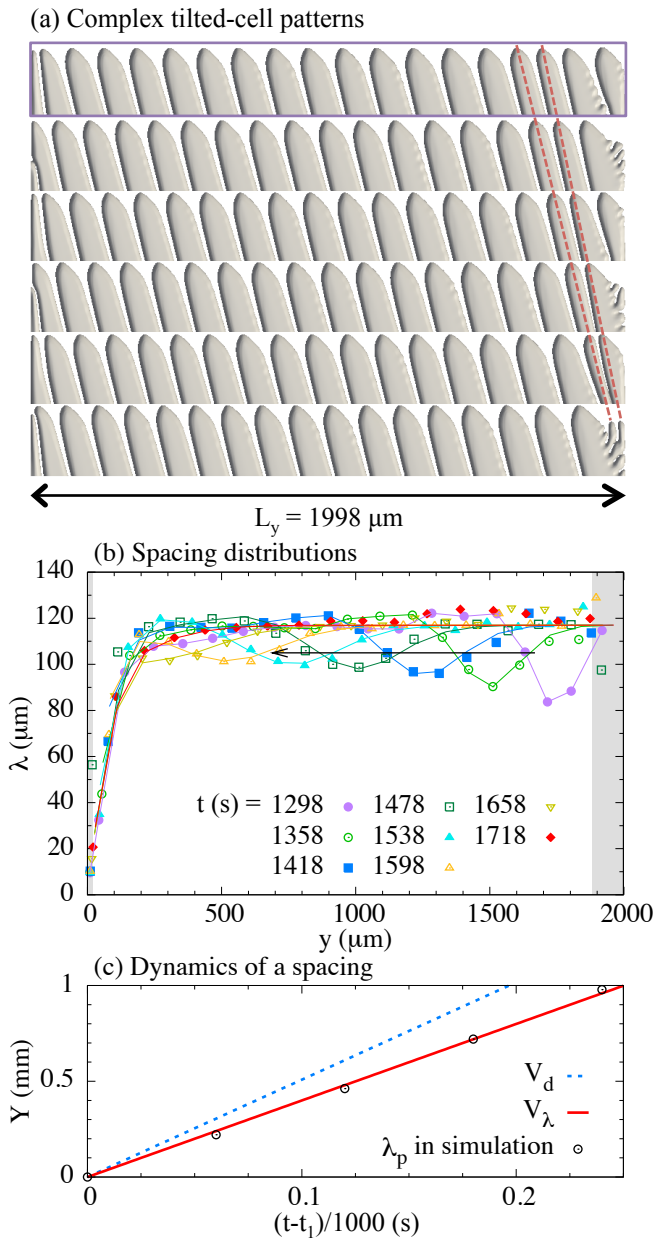

FIG. 8. (a) Tilted-cell arrays during a PF simulation ($\alpha_0 = 15°$; $V = 20\ \mu\mathrm{m\,s^{-1}}$), shown every 12 s from $t = 1238$ s (bottom) to 1298 s (top). The transformation of two incipient sidebranches at the source into two small-spacing cells is highlighted by the two dashed lines. (b) Spacing profiles (symbols) at different times, starting from the top pattern (purple square) of (a). Solid lines: geometrical model (color online for different times). (c) Symbols: spacing propagation $Y(t - t_1)$ for $\lambda_p = 105\ \mu$m from $t_1 = 1358$ s. Solid (dashed) line: linear law with the slope V_λ (V_d).

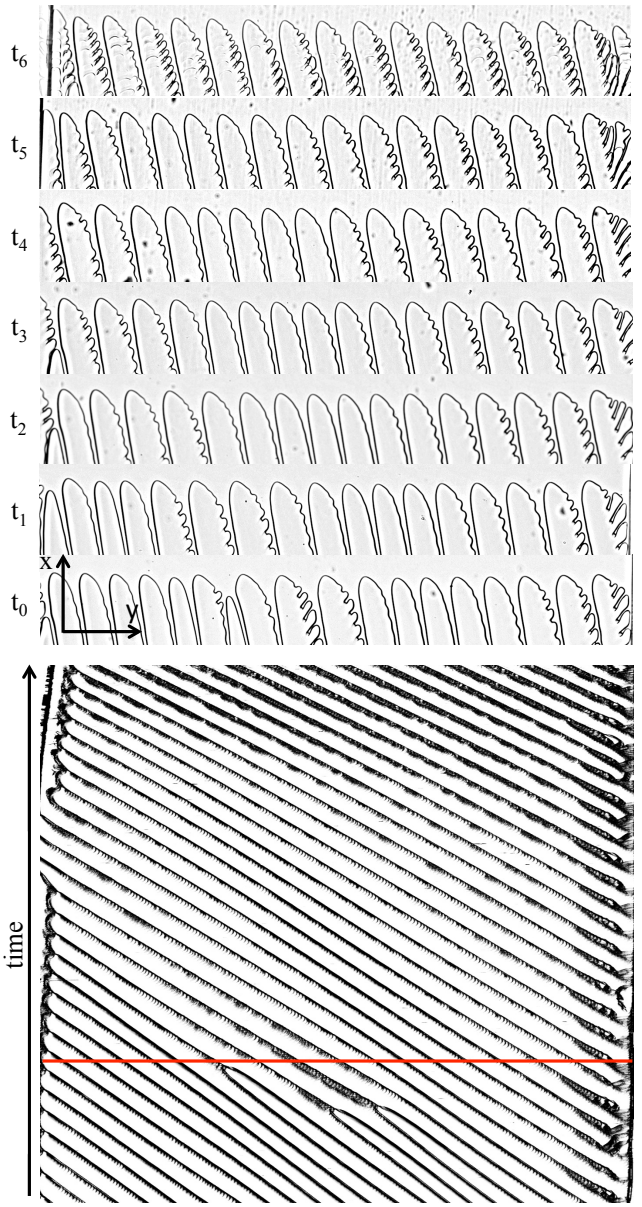

FIG. 9. Tilted-cell array during a directional-solidification experiment in a 100 μm thick sample of a SCN-0.3mol% DC alloy ($V = 4\ \mu\mathrm{m\,s^{-1}}$; $G = 75 \pm 5\ \mathrm{K\,cm^{-1}}$). (a) Snapshots at times $t_0 \approx 4000$ s, $t_1 = t_0 + 600$ s, $t_2 = t_0 + 1350$ s, $t_3 = t_0 + 2100$ s, $t_4 = t_0 + 2850$ s, $t_5 = t_0 + 3600$ s, and $t_6 = t_0 + 4500$ s. (b) Simplified spatiotemporal diagram. Same horizontal dimension as in the snapshots of (a). Vertical dimension: $\approx 6300\ s$ (25.2 mm) of solidification time (length). Horizontal line: time t_0.

was falling between about 8 and 12°, and was thus substantially lower than α_0, as expected. Fig. 9b shows a simplified spatiotemporal diagram corresponding to this experiment (such an image is built by recording a line normal to the growth direction at a fixed position behind the cell tips at regular time intervals, and piled up along an axis representing the time). It reveals that the cellular array is entirely "replaced" by cells created near the source more than twice over the solidification time. As in the PF simulations, new cells are regularly created by tertiary branching (see, e.g., the images at times t_5 and t_6 in Fig. 9a) at the divergent GB source, and elim-

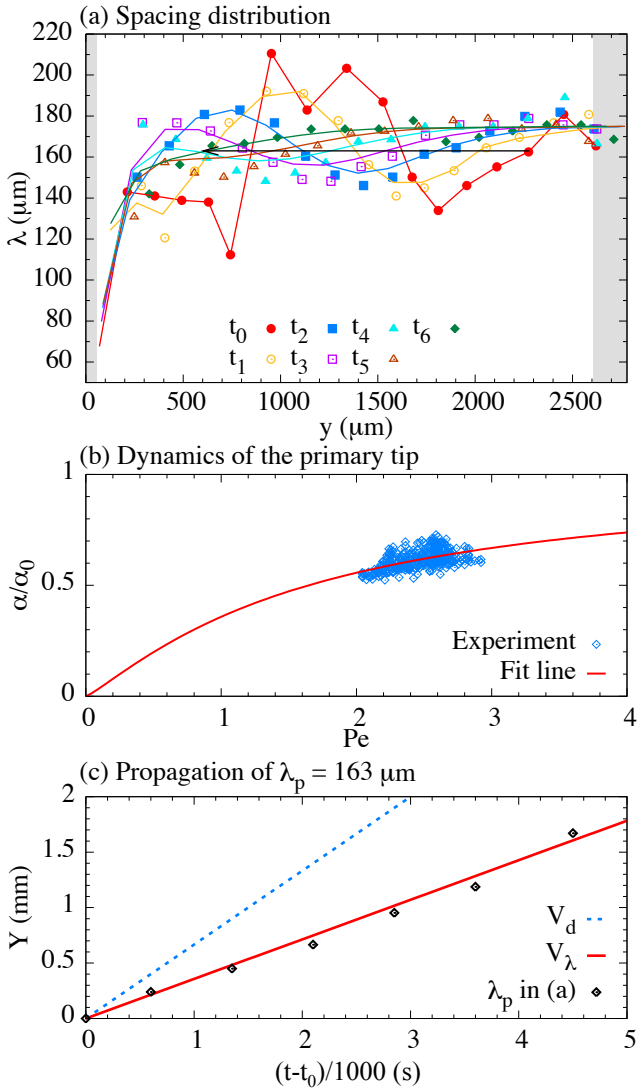

FIG. 10. (a) Symbols: spacing distribution at times t_0 to t_6 during the experiment of Fig. 9. Solid lines: geometrical model. Gray shaded areas: same as in Fig. 5. (b) Symbols: ratio α/α_0 (with $\alpha_0 = 15.5°$) as a function of Pe (measured during the same experiment). Solid line: best-fitting curve using Eq. (3) with $f = 0.558$ and $g = 1.17$. (c) Symbols: abscissa Y corresponding $\lambda_p = 163$ μm as a function of time $t - t_0$. Solid (dashed) lines: slope V_λ (V_d).

inated at the convergent GB sink –one can note some occurrences of a surface dendrite along the sample edge at the convergent GB.

The evolution of the spacing profile from time t_0 to t_6 is shown in Fig. 10a. At t_0, the λ distribution exhibits steep modulations, which are a trace of the cell eliminations during the initial transient. At this stage, the average spacing was relatively close to the value λ_M delivered at the source –this feature contrasts with PF simulations, but is of minor importance as concerns the rest of the dynamics. As in the simulations, the initial modulations of the spacing profile simultaneously smooth out, and are advected laterally towards the convergent GB. Moreover, in the end of the experiment, the spacing profile presents a wide plateau with an essentially uniform spacing λ_M, starting from the source and extending over the major part of the sample, and a narrow region close to the sink, within which the spacing drops.

For further analysis, we measured the dependence of $F(\mathrm{Pe})$ in Eq. (3), as it could be extracted from the modulated patterns during the experiment of Fig. 9. If one refers to the PF simulations (Fig. 3), those data can be expected to be quite close to a $F(\mathrm{Pe})$ law that would characterize perfectly periodic patterns, in spite of their large dispersion (note that producing periodic tilted-cell arrays with various, controlled values of λ is out of reach experimentally). We then used a best-fit procedure for adjusting $F(\mathrm{Pe})$ in Eq. (3) with $D/V = 67.5$ μm to the experimental data. We obtained $f = 0.558$ and $g = 1.17$. The red fitting curve with these parameters in Fig. 10b can describe the experimental measurements (blue diamonds).

We followed the same procedure as above for implementing the geometrical model. We used the spacing profile at t_0 (Fig. 10a) as an initial condition, and set $\lambda_M = 175$ μm and $\lambda_e = 54$ μm. The agreement between the experimental data and the geometrical model is good, in spite of the significantly large uncertainties on the $F(\mathrm{Pe})$ law, and the large amplitude of the initial λ modulations. The profile at the end of the experiment (green diamonds) is quite faithfully reproduced by the geometrical model. We also analysed the spacing propagation by following the abscissa Y corresponding to $\lambda_p = 163$ μm (the black arrow in Fig. 10a). The results are shown in Fig. 10c. Here again, the measured $\mathrm{Y}(t-t_0)$ data (black diamonds) essentially follow a linear variation. In the present case, the slope of this variation is essentially close to the group velocity $V_\lambda = 0.3568$ $\mu\mathrm{m\,s^{-1}}$ (the slope of red continuous line), within experimental accuracy. It is much lower than $V_d = 0.6664$ $\mu\mathrm{m\,s^{-1}}$ (the slope of blue dashed line), as it could be expected from the analysis of the PF simulations.

IV. CONCLUSIONS

We have used thin-sample phase-field (PF) simulations and experiments to investigate the effect of a finite crystal misorientation on the selection of finger-shaped cellular/dendritic array patterns that form during directional solidification of binary alloys. Previous studies have characterized the relationship between the tilt angle α of the pattern and the spacing λ in a situation where λ is spatially uniform[28–33]. The present study focused on the more general situation where the array spacing is *spatially non-uniform*. For a misoriented monocrystal, non-uniformity originates from the creation or elimination of cells at the two lateral edges of the sample and can give rise to different spatial non-uniformities of spacing depending on whether tertiary branching at the divergent

boundary is regular or irregular. Our main finding is that the spatial modulation of spacing propagates laterally at a velocity that is generally slower than the lateral drift velocity $V_d = V \tan\alpha$ of cell/dendrite tips when λ is spatially uniform.

We have shown that this nontrivial behavior follows from the requirement that cells must move so as to conserve their total number away from boundaries. This conservation law yields a continuity equation for the linear density of cells along the array, which transforms into a nonlinear advection equation for the spacing with an advection velocity $V_d - \lambda\, \mathrm{d}V_d/\mathrm{d}\lambda$. The latter is generally less than V_d since the tilt angles, and hence V_d, are monotonously increasing functions of λ. The difference between the two velocities is more pronounced for cells with strong diffusive interactions (Pe $= \lambda V/D$ of order unity) than for well-developed dendrites (Pe $\gg 1$) since the slope $\mathrm{d}V_d/\mathrm{d}\lambda$ is a decreasing function of Pe.

We have further found that, to a good approximation, V_d depends linearly on λ over the limited range of variation of λ when the spacing is non-uniform. This implies that the advection velocity is nearly uniform even when the spacing is non-uniform, and thus that the spatial modulation of spacing is advected in a shape-preserving manner without forming shocks, which generically form when the advection velocity is a strongly varying function of the underlying field as in Burgers' equation[53]. This is best exemplified by the propagation of a front separating regions of large and small uniform spacings when tertiary branching at the divergent boundary is regular. The front propagation thus selects a spacing that is closer to the largest stable spacing λ_{max}, independently of the initial conditions. The selected spacing is generally significantly larger than the initial spacing selected by the transient growth competition between neighboring cells, which falls closer to the smallest stable spacing λ_{min}[15,16,20–22,25].

Front propagation is a relatively slow process, especially for small misorientation since $V \tan\alpha_0$ is an upper bound of the advection velocity. In the present simulations and experiments the time to establish a larger uniform spacing propagatively is at least an order of magnitude larger than the duration of the cell elimination transient leading to the establishment of the initial nonuniform spacing. Therefore, in the light of the present results, the spacing distribution is expected to strongly depend on the duration of the experiment even in the simplest case where tertiary branching at the divergent boundary creates cells with a constant spacing. When tertiary branching at the divergent boundary is irregular so as to create cells with highly variable spacings, the spacing variation can become undulatory. Undulations are advected towards the convergent boundary but also sporadically created at the divergent boundary, such that a steady-state uniform distribution of spacing may never be reached even at arbitrarily large time.

While the present study focused on a misoriented monocrystal, we expect the insights to be relevant for interpreting experimental observations in polycrystals with multiple grains terminated by divergent or convergent grain boundaries. Similarly to the sample edges, those boundaries can act as sources and sinks of cells, respectively. While tertiary branching has been found to depend in a non-trivial way on grain-boundary bicrystallography[30,40], propagation of spacing non-uniformities inside each grain should be governed by the same geometrical model and advection equation developed here for a misoriented monocrystal. The extension of those models to spatially extended three-dimensional patterns is an interesting future prospect.

ACKNOWLEDGMENTS

We thank G. Faivre for fruitful discussions, and P. Ott for her help in the preparation of the experiments. This research was supported by National Aeronautics and Space Administration (NASA) grant NNX16AB54G and by the French Center for Spatial Research (CNES).

APPENDIX A: PHASE DIFFUSION

We performed an independent PF simulation using a well-oriented grain (the upper image of Fig. A1a) in order to obtain an estimate of the phase diffusion coefficient D_λ, independently of any drifitng motion of the cells. For this simulation, we used the same material and numerical parameters as above for a directional-solidification run of a SCN-0.24wt% camphor alloy at $V = 4\ \mu\mathrm{m\,s}^{-1}$ and $G = 19\ \mathrm{K\,cm}^{-1}$ (see Table I). For this purpose, we needed to create a modulated axial-cell array as an initial condition. We carried out a PF simulation with $\alpha_0 = 10°$, and stopped it at time $t = 8000$ s at which (see Fig. 5a) the tilted-cell array was modulated on (twice) the scale of the simulation box. We then abruptly changed the crystal angle to $\alpha_0 = 0°$, and the cells all recovered a well-oriented shape within a time-lapse of approximately 2000 s. We measured the spacing distribution starting from this new $t = 0$ s time (upper image of Fig. A1a) over the whole simulation time. At the final time ($t = 8000$ s, see lower image of Fig. A1a), the pattern was not fully uniform, but the spacing was clearly relaxing towards uniformity with the number of cells and hence the mean spacing λ_m remaining constant in time.

Fig. A1b shows the spacing distribution at $t = 0$ s (blue squares) and $t = 8000$ s (red circles). Except close to the edges, that is, for a system size $L = 2200\ \mu$m comprised between $y_0 = 100\ \mu$m and $y_1 = 2300\ \mu$m (meaning that the gray regions in Fig. A1b are excluded from the analysis), the spacing distribution can be well fitted by a cosine function of the form:

$$\lambda(y,t) = A_\lambda(t) \cos\left(\frac{\pi(y-y_0)}{L} + \phi_0\right) + \lambda_m\,, \qquad \text{(A1)}$$

where $A_\lambda(t)$ is a time-dependent spacing amplitude,

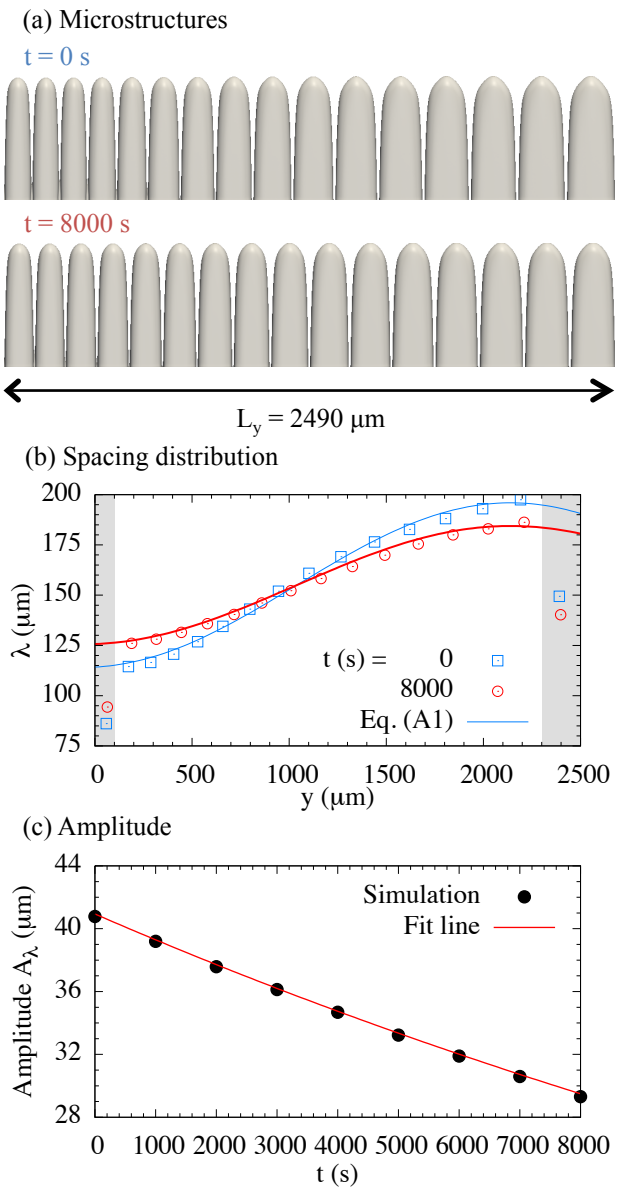

FIG. A1. Relaxation of a non-uniform spacing array. We performed a PF simulation at $V = 4\ \mu\mathrm{m\,s}^{-1}$ and $G = 19\ \mathrm{K\,cm}^{-1}$ using a well-oriented grain (the upper image in a) to estimate a phase diffusivity D_λ. Initial λ relax slowly towards the mean spacing $\lambda_m = 155\ \mu$m over 8000 s (the lower image in a). The simulation measurements (symbols in b) show a cosine distribution Eq. (A1) (continuous lines) away from the boundaries (gray regions in b). We measure the time-dependent spacing amplitude $A_\lambda(t)$ every 1000 s (black circles in a), and the fitting curve (red line in c) of Eq. (A3) with $D_\lambda = 20.1\ \mu\mathrm{m}^2\mathrm{s}^{-1}$ agrees well with the simulation measurements.

while λ_m, y_0, and a phase shift ϕ_0 remain fixed over time. We estimated $\lambda_m = 155\ \mu$m and $\phi_0 = 3.4$. This being defined, we computed $A_\lambda(t)$ every 1000 s from $t = 0$ s to $t = 8000$ s (black circles in Fig. A1c).

Considering a linear-response regime, the relaxation of a smoothly modulated, well-oriented cellular pattern can be described by a diffusion-like equation:

$$\partial_t \lambda = D_\lambda \partial_{yy} \lambda\,. \tag{A2}$$

Our fitting procedure above consists of solving this equation considering the lowest Fourier mode with a wave vector π/L. Accordingly, the time-dependent amplitude $A_\lambda(t)$ is given by:

$$A_\lambda(t) = A_\lambda^0 \exp\left(-\frac{\pi^2 D_\lambda}{L^2} t\right)\,, \tag{A3}$$

where $A_\lambda^0 = 40.9\ \mu$m is the amplitude at $t = 0$ s. Then, D_λ can be estimated using a best-fit adjustment to the $A_\lambda(t)$ data (black circles in Fig. A1c). This yields here $D_\lambda = 20.1\ \mu\mathrm{m}^2\mathrm{s}^{-1}$. The effective diffusion time $L^2/D_\lambda = 310000$ s ($L = 2.5$ mm) is then at least one order of magnitude larger than the values of the time L/V_λ over which a spacing modulation is transported from one edge to the other in tilted-cell patterns, even for small misorientation angles (see Table III). It may be noted that the phase diffusion coefficient in a tilted-cell array may differ from the present value of D_λ, however a quantitative difference is not expected to be as large as questioning substantially our conclusion. In brief, we bring a clear evidence that phase diffusion is essentially negligible as far as the propagative dynamics of tilted-cell patterns is concerned.

[1] M. C. Flemings, *Solidification Processing*, McGraw-Hill, New York (1974).
[2] W. Kurz and D. J. Fisher, *Fundamentals of Solidification*, 3rd ed., Trans Tech, Aedermannsdorf (1992).
[3] J. A. Dantzig and M. Rappaz, *Solidification*, EPFL Press, Switzerland (2009).
[4] W. W. Mullins and R. F. Sekerka, J. Appl. Phys. **35**, 444 (1964).

[5] K. A. Jackson, J. D. Hunt, Acta Metall. **13**, 1212 (1965).
[6] R. Trivedi, K. Somboonsuk, Mater. Sci. Eng. **65**, 65 (1984).
[7] S. Akamatsu and H. Nguyen-Thi, Acta Mat. **108**, 325 (2016).
[8] J. D. Hunt, *Solidification and Casting of Metals*, The Metals Society, London, Book 192, 3 (1979).
[9] K. Somboonsuk, J. T. Mason, and R. Trivedi, Metall. Trans. A **15A**, 967 (1984).
[10] R. Trivedi, Metall. Trans. A **15A**, 977 (1984).
[11] K. Somboonsuk, R. Trivedi, Acta Metall. **33**, 1051 (1985).
[12] R. Trivedi, K. Somboonsuk, Acta Metall. **33**, 1061 (1985).
[13] W. Kurz and D. J. Fisher, Acta Metall. **29**, 11 (1981).
[14] S. H. Han and R. Trivedi, Acta Metall. Meter. **42**, 25 (1994).
[15] J. A. Warren and J. S. Langer, Phys. Rev. E **47**, 2702 (1993).
[16] W. Losert, B. Q. Shi, and H. Z. Cummins, Proc. Natl. Acad. Sci. **95**, 431 (1998).
[17] J. D. Hunt, S.-Z. Lu, Metall. Mater. Trans. A **27A**, 611 (1996).
[18] S.-Z. Lu, J. D. Hunt, J. Cryst. Growth **123**, 17 (1992).
[19] S. Gurevich, A. Karma, M. Plapp, and R. Trivedi, Phys. Rev. E **81**, 011603 (2010).
[20] B. Echebarria, A. Karma and S. Gurevich, Phys. Rev. E **81**, 021608 (2010).
[21] A. J. Clarke, D. Tourret, Y. Song, S. D. Imhoff, P. J. Gibbs, J. W. Gibbs, K. Fezzaa, and A. Karma, Acta Mat. **129**, 203 (2017).
[22] D. Tourret and A. Karma, Acta Mat. **61**, 6474 (2013).
[23] D. Tourret, J.-M. Debierre, Y. Song, F. L. Mota, N. Bergeon, R. Guérin, R. Trivedi, B. Billia, and A. Karma, Phys. Rev. E **92**, 042401 (2015).
[24] J. Pereda, F. L. Mota, L. Chen, B. Billia, D. Tourret, Y. Song, J.-M. Debierre, R. Guérin, A. Karma, R. Trivedi, and N. Bergeon, Phys. Rev. E **95**, 012803 (2017).
[25] M. Greenwood, M. Haataja, and N. Provatas, Phys. Rev. Lett. **93**, 246101 (2004).
[26] T. Haxhimali, A. Karma, F. Gonzales, and M. Rappaz, N. Mat. **5**, 660 (2006).
[27] M. Asta, C. Beckermann, A. Karma, W. Kurz, R. Napolitano, M. Plapp, G. Purdy, M. Rappaz, and R. Trivedi, Acta Mat. **57**, 941 (2009).
[28] S. Akamatsu and T. Ihle, Phys. Rev. E **56**, 4479 (1997).
[29] J. Deschamps, M. Georgelin, and A. Pocheau, Phys. Rev. E **78**, 011605 (2008).
[30] D. Tourret and A. Karma, Acta Mat. **82**, 64 (2015).
[31] J. Li, Z. Wang, Y. Wang, and J. Wang, Acta Mat. **60**, 1478 (2012).
[32] J. Ghmadh, J.-M. Debierre, J. Deschamps, M. Georgelin, R. Guérin, and A. Pocheau, Acta Mat. **74**, 225 (2014).
[33] H. Xing, K. Ankit, X. Dong, H. Chen, and K. Jin, Int. J. Heat Mass Transfer **117**, 1107 (2018).
[34] A. Karma and D. Tourret, Curr. Opin. Solid State Mater. Sci. **20**, 25 (2016).
[35] N. Bergeon, D. Tourret, L. Chen, J.-M. Debierre, R. Guérin, A. Ramirez, B. Billia, A. Karma, and R. Trivedi, Phys. Rev. Lett. **110**, 226102 (2013).
[36] A. Karma and W.-J. Rappel, Phys. Rev. E **57**, 4323 (1998).
[37] A. Karma, Phys. Rev. Lett. **87**, 115701 (2001).
[38] B. Echebarria, R. Folch, A. Karma, and M. Plapp, Phys. Rev. E **70**, 061604 (2004).
[39] K. Glasner, J. Comput. Phys. **174**, 695 (2001).
[40] D. Tourret, Y. Song, A. J. Clarke, and A. Karma, Acta Mat. **122**, 220 (2017).
[41] J. Teng and S. Liu, J. Cryst. Growth **290**, 248 (2006).
[42] S. Liu, J. Teng, and J. Choi, Metall. Mater. Trans. A **38A**, 1555 (2007).
[43] R. Trivedi (private communication).
[44] S. Akamatsu, S. Bottin-Rousseau, M. Perrut, G. Faivre, V. T. Witusiewicz, and L. Sturz, J. Cryst. Growth **118**, 135 (2007).
[45] S. Akamatsu, G. Faivre, and T. Ihle, Phys. Rev. E **51**, 4751 (1995).
[46] B. Kauerauf, G. Zimmermann, L. Murmann, and S. Rex, J. Cryst. Growth **193**, 701 (1998).
[47] V. T. Witusiewicz, L. Sturz, U. Hecht, and S. Rex, Acta Mater. **52**, 5071 (2004); **52**, 5519 (2004); **53**, 173 (2005).
[48] R. N. Grugel and Y. Zhou, Metall. Trans. A **20A**, 969 (1989).
[49] Ch.-A. Gandin, M. Eshelman, and R. Trivedi, Metall. and Meter. Trans. A **27A**, 2727 (1996).
[50] Ch.-A. Gandin and M. Rappaz, Acta Metall. Mater. **42**, 2233 (1994).
[51] H. Esaka, J. Stramke, and W. Kurz, *Columnar Dendrite Growth in Succinonitrile-Acetone Alloys*, Film, Ecole Polytechnique Fédérale de Lausanne, Lausanne, Switzerland (1985).
[52] H. Esaka, W. Kurz, and R. Trivedi, in *Solidification Processing*, J. Beech and H. Jones eds., The Institute of Metals, London, 198 (1988).
[53] J. M. Burgers, *The Nonlinear Diffusion Equation*, D. Reidel Publishing Company, Dordrecht-Boston (1974).
[54] J. Deschamps, Thèse de Doctorat de l'Université Aix-Marseille I (2007).
[55] M. C. Cross and P. C. Hohenberg, Rev. Mod. Phys. **65**, 851 (1993).
[56] J. S. Langer, Phys. Rev. Lett. **44**, 1023 (1980).
[57] S. Akamatsu, M. Plapp, G. Faivre, and A. Karma, Phys. Rev. E **66**, 030501 (2002).